General Bayesian estimation for speckle noise reduction in optical coherence tomography retinal imagery

Alexander Wong[1]*, Akshaya Mishra[1], Kostadinka Bizheva[2], and David A. Clausi[1]

[1]*Dept. of Systems Design Engineering, University of Waterloo, Waterloo, ON N2L3G1, Canada*
[2]*Dept. of Physics and Astronomy University of Waterloo, Waterloo, ON N2L3G1, Canada*
*a28wong@uwaterloo.ca

Abstract: An important image post-processing step for optical coherence tomography (OCT) images is speckle noise reduction. Noise in OCT images is multiplicative in nature and is difficult to suppress due to the fact that in addition the noise component, OCT speckle also carries structural information about the imaged object. To address this issue, a novel speckle noise reduction algorithm was developed. The algorithm projects the imaging data into the logarithmic space and a general Bayesian least squares estimate of the noise-free data is found using a conditional posterior sampling approach. The proposed algorithm was tested on a number of rodent (rat) retina images acquired *in-vivo* with an ultrahigh resolution OCT system. The performance of the algorithm was compared to that of the state-of-the-art algorithms currently available for speckle denoising, such as the adaptive median, maximum a posteriori (MAP) estimation, linear least squares estimation, anisotropic diffusion and wavelet-domain filtering methods. Experimental results show that the proposed approach is capable of achieving state-of-the-art performance when compared to the other tested methods in terms of signal-to-noise ratio (SNR), contrast-to-noise ratio (CNR), edge preservation, and equivalent number of looks (ENL) measures. Visual comparisons also show that the proposed approach provides effective speckle noise suppression while preserving the sharpness and improving the visibility of morphological details, such as tiny capillaries and thin layers in the rat retina OCT images.

© 2010 Optical Society of America

References and links

1. J. Rogowska and M. E. Brezinski, "Evaluation of the adaptive speckle suppression filter for coronary optical coherence tomography imaging," IEEE Trans. Med. Imaging **19**, 1261–1266 (2000).
2. J. Lee, "Speckle suppression and analysis for synthetic aperture radar," Opt. Eng. **25**(5), 636–643 (1986).
3. V. Frost, J. Stiles, K. Shanmugan, and J. Holtzman, "A model for radar images and its application to adaptive digital filtering for multiplicative noise," IEEE Trans. Pattern Anal. Machine Intell. **4**(2), 157–166 (1982).
4. D. Kuan, A. Sawchuk, T. Strand, and P. Chavel, "Adaptive restoration of images with speckle," IEEE Trans. Acoust. Speech Signal Process. **35**(3), 373-383 (1987).

5. T. Loupas, W. Mcdicken, and P. Allen, "An adaptive weighted median filter for speckle suppression in medical ultrasound images," IEEE Trans. Circuits Syst. **36**(1), 129–135 (1989).

6. A. Lopes, E. Nezry, R. Touzi, and H. Laur, "Structure detection and adaptive speckle filtering in SAR images," Int. J. Remote Sens. **14**(9), 1735–1758 (1993).

7. D. C. Adler, T. H. Ko, and J. G. Fujimoto, Speckle reduction in optical coherence tomography images by use of a spatially adaptive wavelet filter, Opt. Lett. **29**(24), 2878-2880 (2004).

8. A. Ozcan, A. Bilenca, A. E. Desjardins, B. E. Bouma, and G. J. Tearney, "Speckle reduction in optical coherence tomography images using digital filtering," J. Opt. Soc. Am. A **24**(7), 1901–1910 (2007).

9. A. Pizurica, W. Philips, I. Lemahieu, and M. Acheroy, "A versatile wavelet domain noise filtration technique for medical imaging," IEEE Trans. Med. Imag. **22**(3), 323–331 (2003).

10. P. Puvanathasan and K. Bizheva, "Speckle noise reduction algorithm for optical coherence tomography based on interval type II fuzzy set," Opt. Express **15**(24), 15747–15758 (2007).

11. S. Aja, C. Alberola, and J. Ruiz, "Fuzzy anisotropic diffusion for speckle filtering," Proc. IEEE ICASSP **2**, 1261–1264 (2001).

12. Y. Yu and S. Acton, "Speckle reducing anisotropic diffusion," IEEE Trans. Image Process. **11**(11), 1260–1270 (2002).

13. P. Puvanathasan and K. Bizheva, "Interval type-II fuzzy anisotropic diffusion algorithm for speckle noise reduction in optical coherence tomography images," Opt. Express **17**(2), 733–746 (2009).

14. D. Fernandez, H. Salinas, and C. Puliafito, "Automated detection of retinal layer structures on optical coherence tomography images," Opt. Express **13**, 10200-10216 (2005).

15. K. Yung, S. Lee, and J. Schmitt, "Phase-Domain Processing of Optical Coherence Tomography Images," J. Biomed. Opt. **4**(1), 125–136 (1999).

16. W. Drexler, "Ultrahigh-resolution optical coherence tomography," J. Biomed. Opt. **9**, 47–74 (2004).

17. J. Schmitt, S. Xiang, and K. Yung, "Speckle in optical coherence tomography," J. Biomed. Opt. **4**, 95–105 (1999).

18. J. Kim, D. Miller, E. Kim, S. Oh, J. Oh, and T. Milner, "Optical coherence tomography speckle reduction by a partially spatially coherent source," J. Biomed. Opt. **10**, 640349 (2005).

19. M. Pircher, E. Gtzinger, R. Leitgeb, A.F. Fercher, and C. K. Hitzenberger, "Speckle reduction in optical coherence tomography by frequency compounding," J. Biomed. Opt. **8**, 565–569 (2003).

20. N. Iftimia, B. E. Bouma, and G. J. Tearney, "Speckle reduction in optical coherence tomography by path length encoded angular compounding," J. Biomed. Opt. **8**, 260–263 (2003).

21. A. E. Desjardins, B. J. Vakoc, W. Y. Oh, S. M. R. Motaghiannezam, G. J. Tearney, and B. E. Bouma, "Angle-resolved Optical Coherence Tomography with sequential angular selectivity for speckle reduction," Opt. Express **15**, 6200-6209 (2007).

22. T. Jorgensen, L. Thrane, M. Mogensen, F. Pedersen, and P. Andersen, "Speckle reduction in optical coherence tomography images of human skin by a spatial diversity method," in Proc. SPIE 6627, Munich, Germany 66270P (2007).

23. J. Schmitt, "Array detection for speckle reduction in optical coherence microscopy," Phys. Med. Biol. **42**(7), 1427–1439 (1997).

24. M. Bashkansky and J. Reintjes, "Statistics and reduction of speckle in optical coherence tomography," Opt. Lett. **25**, 545-547 (2000).

25. D. Popescu, M. Hewkoa, and M. Sowa, "Speckle noise attenuation in optical coherence tomography by compounding images acquired at different positions of the sample," Opt. Comm. **1**(1), 247–251 (2007).

26. M. Kobayashi, H. Hanafusa, K. Takada, and J. Noda, "Polarization-Independent Interferometric Optical-Time-Domain Reflectometer," J. Lightwave Technol. **9**, 623–628 (1991).

27. W. Hastings, "Monte carlo sampling methods using Markov chains and their applications," Biometrika **57**(1), 97–109 (1970).

28. P. Puvanathasan, P. Forbes, Z. Ren, D. Malchow, S. Boyd, and K. Bizheva, "High-speed, high-resolution Fourier-domain optical coherence tomography system for retinal imaging in the 1060 nm wavelength region," Opt. Lett. **33**(21), 2479–2481 (2008).

1. Introduction

Speckle is an inherent characteristic of images acquired with any imaging technique that is based on detection of coherent waves, for example synthetic aperture radar (SAR), ultrasound, coherent optical imaging, etc. Speckle carries information about both the structure of the imaged object as well as a noise component, and the latter is responsible for the grainy appearance of the images. Optical coherence tomography (OCT) is an imaging technique capable of non-contact, high resolution (few micrometers), 3D imaging of the structure of optically semitransparent objects, including biological tissue. Since OCT is based on interferometric detection of coherent optical beams, OCT images contain speckle. Speckle in OCT tomograms is dependent

on both the wavelength of the imaging beam and the structural details of the imaged object [1].

With the development of ultrahigh resolution OCT (UHROCT), cellular level resolution can be achieved in biological tissue. This enables the visualization of small morphological details in the UHROCT tomograms such as individual tissue layers, small blood and lymph vessels, calcifications, lipid deposits, small clusters of highly specialized cells, etc. Such small structural details can easily be obscured by the presence of speckle noise in unprocessed UHROCT images, or by the blurring and / or image artefacts introduced by speckle denoising algorithms that are currently used in commercial and research grade OCT systems or have been published in the past. Furthermore, the development of high speed UHROCT technology permits fast acquisition of high density, large volume 3D images of biological tissue. The development of fast speckle noise reduction algorithms for UHROCT with very good preservation of boundaries of layered structure or small morphological features is of high importance. Such algorithms can improve the quality of the visual appearance of UHROCT images and allow for zooming on small features in the image without compromising the sharpness of the details or the overall image quality. Furthermore, speckle noise reduction algorithms can potentially improve the precision and overall performance of other image post-processing algorithms such as layer segmentation and pattern analysis that are often applied to UHROCT images for quantitative analysis. However, speckle noise reduction in OCT images is particularly challenging, because of the difficulty in separating the noise and the information components in the speckle pattern.

Many methods have been proposed over the years to tackle the challenge of speckle noise reduction both for OCT and other imaging methods. Linear least-squares estimation methods based on local statistics [2–4] and adaptive median filtering [5] were first employed for reducing speckle noise. These methods provide insufficient noise reduction under high speckle noise contamination, as well as result in significant loss of detail, which is undesirable for clinical retinal analysis. Filtering approaches based on the rotating kernel transform [1] have been shown to provide better contrast, however these methods suffer from significant loss of structural details in the case of high level of speckle contamination. Maximum a posteriori (MAP) estimation approaches [6] have also been investigated for speckle noise reduction. Since these methods rely on specific parametric noise distribution models, they are ill-suited in situations where the noise distribution model is unknown. In recent years, two classes of approaches have been heavily investigated for speckle noise reduction. The first class of approaches that became popular in recent years for speckle noise reduction are wavelet-based methods [7–10], where the data undergoes multi-scale decomposition using wavelet transforms and wavelet coefficients associated with the speckle noise are suppressed in the individual sub-bands. While wavelet-based methods provide improved speckle noise suppression and reduced detail loss compared to earlier approaches, such methods can introduce significant artefacts that relate to the choice of wavelet used. The image artefacts can obscure or reduce the visibility of fine structural details, thus reducing the overall image quality of the UHROCT tomograms. The second class of approaches that has gained popularly in recent years for speckle noise reduction are anisotropic diffusion-based methods [11–14]. While such methods provide improved noise suppression and reduced detail loss as compared to traditional methods and do not introduce artefacts into the processed images as the wavelet-based methods do, they provide limited speckle noise suppression under high speckle noise contamination, which is often the case with OCT retinal images. All of the above algorithms do not deliver sufficient noise suppression under high speckle contamination for two main reasons. First, these methods use a small number of pixels to estimate the original signal, which does not provide sufficient information for accurate estimation under high speckle noise contamination. Second, these methods do not learn the underlying noise statistics from the noise-contaminated images and do not account for the complex nature of OCT imagery, which is important for accurate estimation under high speckle

noise contamination. Hybrid methods that require both acquisition and algorithmic processes have also been introduced, such as the phase domain processing and zero-adjustment procedure proposed by Yung et al. [15].

In addition to algorithmic approaches to speckle noise reduction, design changes to the OCT imaging technique have been proposed to reduce the presence of speckle noise on the imaging side. Kim et al. [18] proposed the use of a partially spatially coherence broadband light source to reduce the presence of speckle noise. Pircher et al. [19] proposed a frequency compounding method which makes use of two incoherent interferometric signals to reduce speckle noise while maintaining high spatial resolution. Iftimia et al. [20] proposed an angular compounding approach based on path length encoding, which was also found to reduce the presence of speckle noise. More recently, Desjardins et al. [21] was able to achieve speckle noise reduction through the use of angular compounding at multiple backscattering angles. Finally, Jorgensen et al. [22] proposed a spatial diversity approach, where the probe beams focal plane is shifted to achieve speckle reduction. Other spatial diversity based approaches [23–25], as well as polarization diversity based approaches [26] have also been investigated. However, such methods require significant changes to the design of the OCT system, longer data acquisition time and in most cases the effect of speckle denoising is limited. Therefore, the development of algorithmic approaches to speckle noise reduction remains an important part of the OCT images post-processing.

Here we present a novel speckle noise reduction algorithm based on nonlinear log-space general Bayesian least squares estimation. The novelty of the algorithm stems from the conditional posterior sampling approach used to estimate the posterior distribution of the noise-free data in a non-parametric fashion. This allows the algorithm to learn the underlying noise distribution of the observed data dynamically to provide significant speckle noise suppression while preserving image details. When applied to UHROCT images, acquired *in-vivo* from rodent (rat) retinas, the novel algorithm shows significantly improved overall image quality and clear preservation of small structural features in the retinal images.

2. Theory

Let S be a set of sites on a discrete lattice $\mathscr{L}$ which defines an OCT image and let $s \in S$ be a site in $\mathscr{L}$. Let $M = \{M(s)|s \in S\}$, $A = \{A(s)|s \in S\}$, and $N = \{N(s)|s \in S\}$ be fields on S. Given the measured data $M(s)$ that we have acquired, let $A(s)$ and $N(s)$ be random variables representing noise-free data and speckle noise of unknown distribution at site s respectively. Let $m = \{m(s)|s \in S\}$, $a = \{a(s)|s \in S\}$, and $n = \{n(s)|s \in S\}$ be realizations of M, A, and N respectively. Speckle in OCT imagery arises from the constructive and destructive interference of the backscattered signal from biological issues [16], and can be modeled as multiplicative noise that is dependent on the wavelength of the imaging beam and the structural composition of the imaged object [17],

$$m(s) = a(s) \cdot n(s). \tag{1}$$

The data-dependent nature of speckle noise, as well as the fact that the speckled noise distribution can vary depending on the optical design of the imaging system, makes the problem of separating the noise-free data $a(s)$ from the speckle noise $n(s)$ very challenging. We propose to tackle these issues associated with speckle noise reduction by estimating the noise-free data in the logarithm space using a general Bayesian least squares estimation approach based on conditional posterior sampling. The proposed speckle noise reduction algorithm can be described as follows. To handle the data-dependent nature of speckle noise, the noise-free data $a(s)$ and the speckle noise $n(s)$ are decoupled by projecting the measured data $m(s)$ into the logarithm space,

$$\log m(s) = m_l(s) = \log[a(s) \cdot n(s)] = log\{a(s)\} + log\{n(s)\} = a_l(s) + n_l(s). \qquad (2)$$

In the logarithm space, the general Bayesian least squares estimate of $a_l(s)$ can be defined by the expression,

$$\hat{a}_l(s) = \underset{a_l(s)}{\arg\min}\left\{ E\left[(a_l(s) - \hat{a}_l(s))^2 \,|m_l(s)]\right]\right\}. \qquad (3)$$

What the general Bayesian least squares estimate does is minimize the average squared error of the noise-free data estimate $\hat{a}_l(s)$ based on the measured data $m_l(s)$. Minimizing the expression in Eq. (3) gives,

$$\hat{a}_l(s) = \int p\left(a_l(s)|m_l(s)\right)a_l(s)da_l(s). \qquad (4)$$

What the expression in Eq. (4) shows is that the optimal Bayesian estimate of the noise-free data $a_l(s)$ is essentially the statistical average based on the measured data $m_l(s)$. The posterior distribution $p\left(a_l(s)|m_l(s)\right)$, which represents the probability distribution of the noise-free data $a_l(s)$ based on the knowledge of the measured data $m_l(s)$, can be highly complicated and non-linear in nature, making it difficult to solve for $\hat{a}_l(s)$ using Eq. (4). Typically, simpler Bayesian linear least squares estimators [2] and estimators based on specific parametric posterior distribution models [6] have been used instead for speckle noise reduction. However, given the complex nature of the OCT images, such estimators provide poor signal-noise separation and hence result in significant loss of structural detail. To address these issues, we propose to employ a conditional posterior sampling approach to estimate $p\left(a_l(s)|m_l(s)\right)$.

What conditional posterior sampling does is select information from the measured data $m_l(s)$ to estimate the posterior distribution $p\left(a_l(s)|m_l(s)\right)$ based on conditions that identify the relevance of that information to accurate estimation. For example, when estimating the posterior distribution of a pixel with strong boundary characteristics, conditional posterior sampling adaptively selects information from the measured data that has similar boundary characteristics to estimate the posterior distribution, as that would allow the boundary characteristics to be preserved while averaging out the speckle noise.

The conditional posterior sampling approach we used to estimate $p\left(a_l(s)|m_l(s)\right)$ can be described as follows. In Markov-Chain Monte Carlo density estimation [27], an unknown target distribution (in our case, $p\left(a_l(s)|m_l(s)\right)$) is estimated in an indirect manner by first sampling from a known initial probability distribution Q. Similarly, in the proposed approach, a random site s' in S is determined based on an initial probability distribution $Q(s'|s)$. $Q(s'|s)$ is defined as a Gaussian distribution centered at s,

$$Q(s'|s) = \frac{1}{2\pi\sigma_{\text{spatial}}}e^{-\left(\frac{\|s'-s\|^2}{2\sigma_{\text{spatial}}^2}\right)}, \qquad (5)$$

where $\|s'-s\|^2$ denotes the squared Euclidean distance of a site s' from s, and σ_{spatial} represents the spatial variance of the initial probability distribution $Q(s'|s)$, which is set to 7 pixels as it was shown to provide accurate estimates during testing. Testing under different imaging conditions as well as different resolutions have shown that the use of $\sigma_{\text{spatial}} = 7$ allows for consistently accurate results, thus making that setting suitable for a wide range of imaging scenarios. The reason for the strong performance using this setting is that the algorithm is adapts to the underlying statistics of the image and as such performs well as long as the selected area to select samples from is large enough to obtain good statistics from, irrespective of the resolution of the image. This initial probability distribution $Q(s'|s)$ generates sites that tend to be in closer

proximity to site s. Given the drawn site s', the inclusion of s' as a realization of $p\left(a_l(s)|m_l(s)\right)$ is determined based on the condition,

$$\left|\mu\left(s\right) - \mu\left(s'\right)\right| < 2\sigma, \qquad (6)$$

where $\mu(s)$ is the local mean of the neighborhood centered at s and σ is the estimated image noise variance. The local mean $\mu(s)$ is computed in a 7×7 region centered at s in the current implementation, as that provides sufficient information to obtain good statistics from, irrespective of the resolution of the image. Furthermore, in the current implementation of the proposed method, the noise variance σ was estimated by taking the local variance within a 7×7 region for the same reason of obtaining good statistics. Equation (6) enforces the inclusion of s' as a realization of $p\left(a_l(s)|m_l(s)\right)$ within two standard deviations, which accounts for the effect of noise variations. The inclusion of s' as a realization of $p\left(a_l(s)|m_l(s)\right)$ is based on the assumption that the local mean is a reasonable initial estimate of $a_l(s)$. This conditional sampling is repeated until the maximum number of sites used to estimate the original signal, denoted as γ, is drawn.

Given the set of γ sites drawn from $Q(s'|s)$, denoted as $\Omega = \{s'_1, s'_2, \ldots, s'_\gamma\}$, the weight associated with each site s'_i in estimating $a_l(s)$, denoted as $w(s'_i|s)$, is computed using the following Gibbs-based likelihood function based on the local means of s'_i and s,

$$w\left(s'_i|s\right) = \exp\left[-\left(\frac{\left|\mu\left(s'_i\right) - \mu\left(s\right)\right|}{2\sigma^2}\right)\right]. \qquad (7)$$

Equation (7) allows for a more reliable estimate of $p\left(a_l(s)|m_l(s)\right)$ by weighing sites with local means similar to the local mean of site s higher since they are more likely to be true realizations of $p\left(a_l(s)|m_l(s)\right)$.

Given a set of sites $\Omega = \{s'_1, s'_2, \ldots, s'_\gamma\}$ and the associated set of weights $W = \{w(s'_1, s), w(s'_2, s), \ldots, w(s'_\gamma, s)\}$, the posterior distribution $p\left(a_l(s)|m_l(s)\right)$ is then estimated using a weighted histogram approach. Suppose that the discrete range of possible measured data values (m_l) be $[L_{\min}, L_{\max}]$, where $L_{\min}$ and $L_{\max}$ are the minimum and maximum possible values, respectively. Let the discrete range of possible noise-free data values (a_l) also be $[L_{\min}, L_{\max}]$. Furthermore, let $h(r_k)$ be a weighted histogram, defined over $[L_{\min}, L_{\max}]$, where r_k is the kth possible noise-free data value. For each site s'_i, the weight $w(s'_i|s)$ is accumulated in the histogram bin of the weighted histogram that corresponds to $m_l(s'_i)$ (i.e., $h(r_k = m_l(s'_i))$). After constructing the weighted histogram, each histogram bin is then divided by the sum of all weights to construct a normalized histogram representing $p\left(a_l(s)|m_l(s)\right)$. Therefore, $\hat{p}\left(a_l(s)|m_l(s)\right)$ can be formulated as

$$\hat{p}\left(a_l(s)|m_l(s)\right) = \frac{\sum\limits_{k=\Omega} w\left(s'_k|s\right)\delta\left(a_l - m_l(s'_k)\right)}{Z}, \qquad (8)$$

where $\delta(.)$ is the Dirac delta function and Z is a normalization term such that $\sum\limits_{a_l}\hat{p}\left(a_l(s)|m_l(s)\right) = 1$.

Finally, the estimate of $a(s)$ can be found by back-projecting the Bayesian estimate of $a_l(s)$ computed using the estimated $p\left(a_l(s)|m_l(s)\right)$ [Eq. (4)] from the logarithm space using $\hat{a}(s) = \exp\left[\hat{a}_l(s)\right]$. A flowchart detailing a step-by-step breakdown of the proposed despeckling algorithm is shown in Fig. 1.

3. Results and discussion

To evaluate the effectiveness of the proposed log-space general Bayesian estimation approach for speckle noise suppression in OCT tomograms, the method was applied to a set of UHROCT
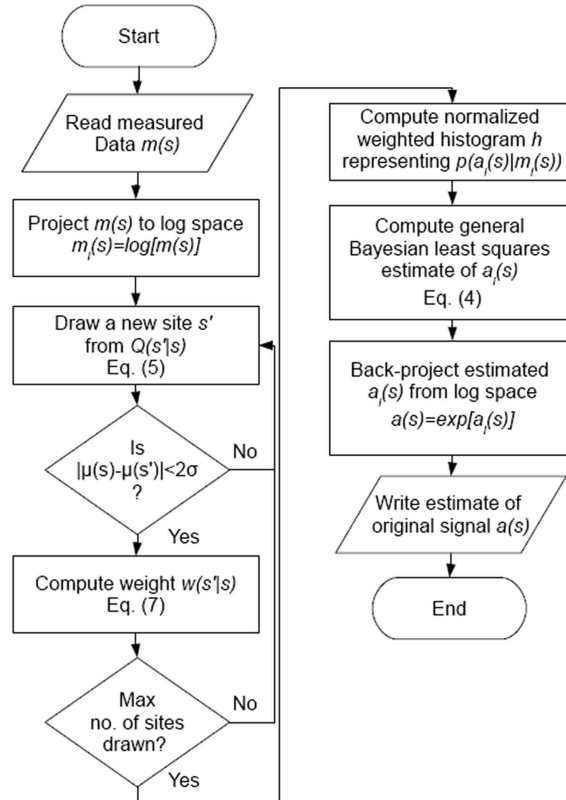
Fig. 1. Step-by-step flowchart of the proposed despeckling algorithm.

images of the rat retina acquired *in-vivo* with a research grade UHROCT system. Two representative images acquired at and away from the optic disc of the rat eye (Fig. 2) are discussed.

The images were acquired with a state-of-the art, research grade high speed, UHROCT system operating in the 1060nm wavelength region. A detailed description of the system can be found in [28]. Briefly, the UHROCT system is based on a spectral domain design powered with a super-luminescent diode (λc = 1020nm, $\delta\lambda$ = 110nm, P_{out} = 10mW) and data is acquired with a 47kHz data rate, InGaAs linear array, 1024 pixel camera (SUI, Goodrich) interfaced with a high performance spectrometer (P&P Optica). The UHROCT system provides $3\mu m$ axial and $5\mu m$ lateral resolution in retinal tissue and 100dB SNR for 1.3mW optical power incident on the rat cornea.

2D and 3D images were acquired from the retinas of living Long Evans rats and the imaging procedure was carried out in accordance with the University of Waterloo ethics regulations. The two selected images, one acquired at the optic disc of the retina [Fig. 2(a)], and one 2mm away from the optic disc [Fig. 2(b)], containing different morphological features, were selected to test the performance of the speckle noise reduction algorithm. Both images show clear visualization of all intraretinal layers, as well as small morphological details such as the tiny capillaries (10μm in diameter) in the inner- and outer plexiform layers (red arrows) and the larger choroidal blood vessels (yellow arrows). For comparison purposes, the same images were also processed with some of the high performance wavelet- or diffusion-based image processing algorithms, such as the adaptive median filter proposed by Loupas et.al. [5], the linear least
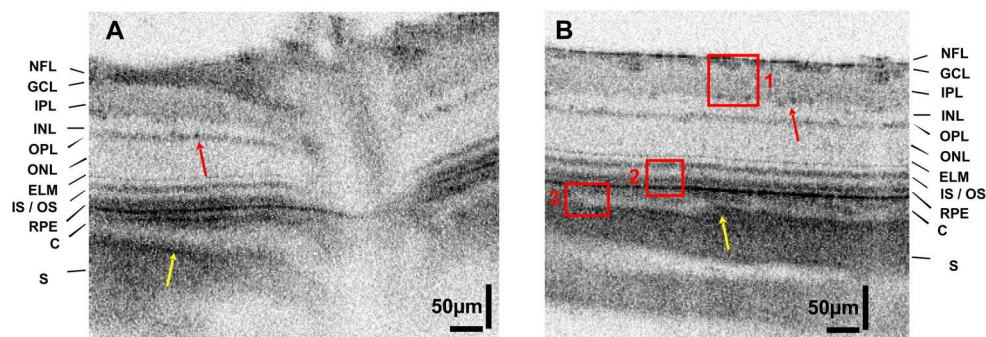
Fig. 2. UHROCT images of the rat retina acquired near the optic disc (A) and away from the optic disc (B). NFL nerve fiber layer; GCL ganglion cell layer; IPL inner plexiform layer; INL inner nuclear layer; OPL outer plexiform layer; ONL outer nuclear layer; ELM external limiting membrane; IS inner segment; OS outer segment of the photoreceptor layer; RPE retinal pigmented epithelium; C- choroid and S sclera. The red arrows mark tiny capillaries imbedded in the retinal OPL, while the yellow arrows mark large blood vessels in the choroid. The red line boxes mark sections of the retinal image that were enlarged for more direct visual comparison of the performance of the speckle denoising algorithms (see Figs. 3,4 and 5).

squares estimator proposed by Frost et al. [3], the wavelet-based method proposed by Pizurica et al. [9], the MAP method proposed by Lopes at el. [6], the anisotropic diffusion method proposed by Yu and Acton [12], and the Type II Fuzzy anisotropic diffusion method proposed by Puvanathasan and Bizheva [13]. All tested methods were implemented in as computationally efficient a manner as possible, using the parameters proposed in the associated research literature. For the proposed method, the number of sites used to estimate the original signal at each site, denoted as γ, was set to 64 and 7×7 neighborhoods were used, as they were proven to produce good estimates of $p(a_l(s)|m_l(s))$. Tests performed under different imaging conditions, resolutions, as well as biological tissues other than retina (e.g., corneal and skin) and the testing have shown that selection of these parameters work well for a wide variety of different imaging scenarios. The reason for the strong performance using such parameters is that the proposed algorithm adapts to the underlying statistics of the image and as such performs well as long as the selected area to select samples from is large enough to obtain good statistics from, irrespective of the resolution of the image. As such, the use of the presented parameters should provide strong speckle noise reduction performance for most practical situations. All algorithms were implemented in MATLAB and tested on an Intel Pentium 4, 3 GHz machine with 1 GB of RAM. For direct comparison of the algorithms performance, 3 regions of the retinal image [Fig. 2(b)] were selected (red-line boxes), focusing on specific morphological features such as the retinal capillaries and surface blood vessels (box #1), the boundaries between retinal layers (box #2), the choroidal blood vessels (box #3). Significant efforts were made to ensure fair comparisons between the proposed algorithm and other tested speckle denoising algorithms. Extensive parametric testing showed that the parameters proposed in the associated research literature for the tested algorithms provide the strongest results that can be obtained using these methods for the tested retinal images, as changes to these parameters yield no improvements in terms of the results.

Figure 3 shows qualitative, visual comparisons of the original and processed UHROCT retina

images acquired away from the optic disc. All retinal layers, as well as small features, such as the tiny capillaries imbedded in the inner plexiform layer of the retina (red arrows) and choroidal blood vessels (yellow arrows) are visible in the image. Blue and red coloured, numbered boxes in the original images mark the regions of interest used in the quantitative comparison of the processed images described below. Although morphological features are visible in the images, presence of speckle noise causes the grainy appearance of the UHROCT unprocessed tomogram. As a result, segmentation algorithms applied to this image may fail to identify properly the boundaries of all retinal layers, specifically the thin retinal layers such as the external limiting membrane (ELM) and the inner plexiform layer (IPL), as well as to define well the inner boundaries of the choroidal blood vessels. Precise determination of choroidal and retinal blood vessels diameter is essential for the accurate calculation of retinal blood flow.

Visual comparison of the processed images reveals that the adaptive median filter (AMF) preserved image detail but provided limited noise suppression. The linear least squares estimation method (LLSQ) provided better noise suppression but at the cost of significant loss of image detail. The wavelet noise reduction methods provided both improved noise suppression and detail preservation, but introduced wavelet related artefacts (Fig. 4). The MAP and anisotropic diffusion (AD) methods provided good noise suppression and detail preservation with minimal appearance of image artefacts. In contrast, application of the proposed method resulted in noticeably improved detail preservation and noise suppression compared to the other tested methods. Areas with fairly homogeneous structure, for example the inside of the inner and outer nuclear layers, as well as part of the sclera [see regions marked with red numbered boxes in Fig. 2(b)] show excellent removal of the grainy appearance characteristic of the original image and most of the other post-processed images and associate with presence of speckle noise. While the speckle noise removal with the new algorithm results in blurring of the homogenous regions of the image, image features corresponding to actual morphological details in the retina remain very well preserved and show improved visibility (contrast).

To emphasize the difference in edge preservation and contrast improvement between the proposed method and the other algorithms, three regions in the original image [Fig. 2(b)] were selected and marked with red line, numbered boxes, and enlarged views of these regions are shown in Figs. 4, 5, and 6. These regions were chosen to contain image details such as very thin retinal layers, tiny capillaries and cross-sections of larger retinal and choroidal blood vessels, in order to evaluate the performance of the individual algorithms under different conditions.

Figure 4 shows a section of the original image [Fig. 2(b)] marked with red box #1, containing a cross-section of a large blood vessel imbedded in the NFL, and the cross-sections of three capilaries positioned at the interface between the IPL and INL. The original inset shows that the presence of speckle noise reduces the image quality to the extent that the cross-section of the second (middle) capillary is barely visible, while the outlines of the rest of the blood vessels appear blurred. The application of the AMF algorithm does not improve image quality significantly, while the LLSQ method blurs the image to the extent that the outlines of blood vessel cross-sections cannot be easily distinguished. Both the AD and wavelet methods improve the overall contrast of the image and the visibility of the blood vessel cross-sections, however these methods introduce significant artefacts in the processed images that blur the contours of the blood vessel cross-sections. Both the MAP and the Type II Fuzzy AD approaches appear to significantly improve the contrast and visibility of the blood vessel cross-sections, but some residual blur is still present in the contours of the cross-sections.

The proposed algorithm removes speckle noise from the homogeneous regions of the IPL and INL layers and greatly improves the contrast and visibility of the image features. Furthermore, the edge preservation of this method is effective, as the outlines of all blood vessels appear sharp and well defined.
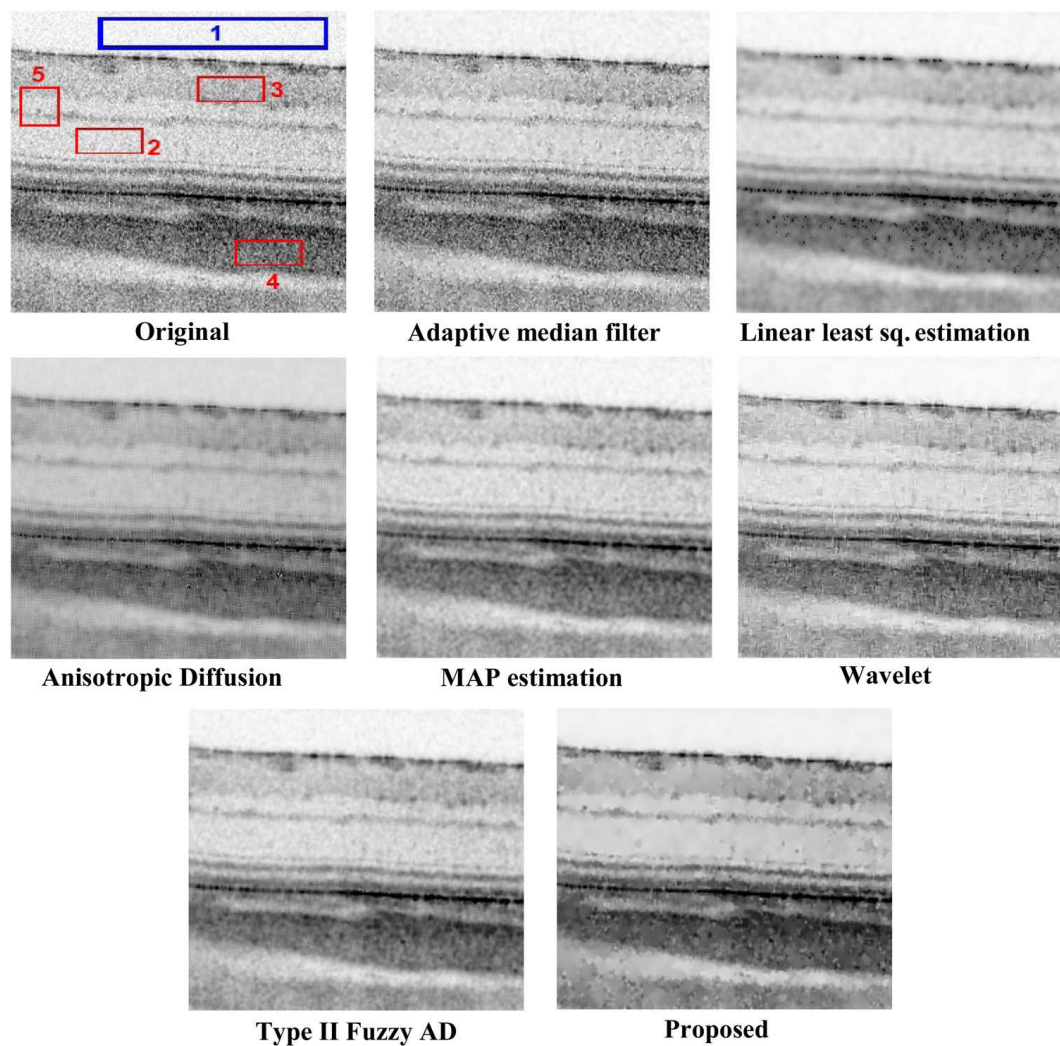
Fig. 3. An OCT image of the rat retina acquired away from the optic disc and processed with the following filters: Original image, Adaptive median filter, Linear least square estimation, Anisotropic Diffusion, MAP estimation, general Wavelet, Type II Fuzzy AD, and the new proposed algorithm. The blue and red-line boxes in the original image mark regions in the image used for quantitative comparison of the performance of all image processing algorithms applied to the original image.

Figure 5 shows a region of the original image [Fig. 2(b)] marked with red box #2, containing sections of the RPE layer (thin black line) and the IS / OS portion of the photoreceptor layer (pale and dark gray alternating layers). The original inset shows that the presence of speckle noise reduces the overall image quality and blurs the boundaries of the individual layers. The application of other tested algorithms causes significant blur of the layers boundaries and in the case of the AD and Wavelet methods, introduces image artefacts. Overall, the best performance in terms of improved image contrast and visual appearance, and best edge preservation with practically no image artefacts, for the case of layered structures in the UHROCT image is achieved with the proposed algorithm.

Figure 6 shows the performance of the different algorithms in terms of improving the appearance of choroidal blood vessels to allow for more precise segmentation and measurement of the blood vessel diameter. For this purpose, we have selected a region in the original image [Fig. 2(b)] marked with red box #3, that contains a part of the blood vessel longitudinal cross-section. The presence of speckle noise in the original image in Fig. 6 blurs the contours of the blood vessel to the extent that precise determination of the blood vessel diameter is not possible. The application of the AMF algorithm does not improve image quality significantly. The LLSQ, MAP and Fuzzy type II AD algorithms result in significantly improved contrast between the blood vessels and the surrounding choroidal tissue, at the expense of significant blur of the blood vessel contours, which is most extreme in the case of the LLSQ method. Although the Wavelet approach results in the best contrast improvement, it introduces image artefacts that can compromise the overall visual appearance of the processed image. Both significant blur and image artefacts are present in the image processed with the AD method. The proposed approach generates an optimal combination of improved image contrast, visual appearance and sharp boundaries of the blood vessel cross-section.

Figure 7 shows qualitative, visual comparison of the original and processed OCT retina images acquired at the optic disc of the rat retina [Fig. 2(a)]. Again, all intra-retinal layers, as well as small features, such as tiny capillaries imbedded in the inner plexiform layer of the retina, and choroidal blood vessels are visible in the image. The cross-section of the remains of the hyaloids blood vessel is also visible. Blue and red colored, numbered boxes mark the regions of interest used in the quantitative comparison of the processed images described below. In addition to improving the visual appearance of the layered retinal structure, as in Fig. 2, here the novel speckle noise reduction algorithm results in better visualization of the outline of the optic disc funnel, as well as clearly defined inner and outer boundaries of the hyaloid blood vessel. The interface between the retinal nerve fiber layer (RNF) and the IPL is also significantly sharper with better contrast as compared to the original and the rest of the processed images. The sharper appearance of the optic disc funnel and overall layered retinal structure can aid and significantly improve the performance of automatic segmentation algorithms targeting to evaluate the RNF thickness and optic disc diameter in healthy and diseased retinal images. Quantitative analysis of the RNFL thickness and the dimensions of the optic disk are used in clinical studied for improved and early diagnostics of glaucoma.

To compare the tested methods in a quantitative manner, the average SNR, contrast-to-noise ratio (CNR), equivalent number of looks (ENL), and edge preservation (η) over the *in-vivo* OCT retinal images were computed for each tested method. The image quality metrics used are the same as the metrics used in [7, 10, 13], and are defined as follows:

$$SNR = 10\log_{10}\left[\max(A^2)/\sigma^2\right], \tag{9}$$

$$ENL = \frac{1}{H}\left[\sum_{h-1}^{H}\frac{\mu_h^2}{\sigma_h^2}\right], \tag{10}$$

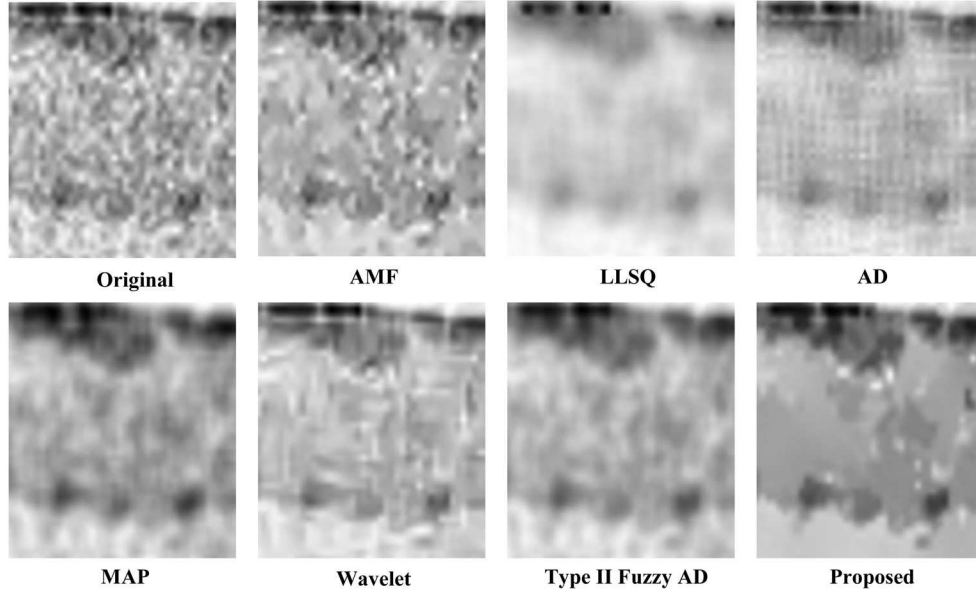| Original	AMF	LLSQ	AD
MAP	Wavelet	Type II Fuzzy AD	Proposed

Fig. 4. 3X enlargement of the region in the original OCT image marked with the red box #1 in Fig. 1(b) and processed with the following filters: AMF (adaptive median filter); LLSQ (linear least square estimation); AD (adaptive diffusion); general Wavelet; MAP (maximum a posteriori estimation); Type II fuzzy AD (fuzzy rules controlled adaptive diffusion). Features in the original image such as the large blood vessel in the NFL and the three capillaries positioned at the boundary between the IPL and INL appear very sharp and distinct on the image processed with the proposed algorithm. In contrast, the same image features appear with low contrast and blurred boundaries on the images processed with the rest of the algorithms.

$$CNR = \frac{1}{R}\left[\sum_{r=1}^{R}\frac{(\mu_r - \mu_b)}{\sqrt{\sigma_r^2 + \sigma_b^2}}\right],\tag{11}$$

$$\eta = \frac{\sum\left(\nabla^2 M - \overline{\nabla^2 M}\right)\left(\nabla^2 A - \overline{\nabla^2 A}\right)}{\sqrt{\sum\left(\nabla^2 M - \overline{\nabla^2 M}\right)^2 \cdot \sum\left(\nabla^2 A - \overline{\nabla^2 A}\right)^2}},\tag{12}$$

ENL measures the smoothness of a homogenous region of interest, while CNR measure the difference between an area of image feature and an area of background noise. Edge preservation is a correlation measure that indicates how the edges in the image are degrading. A value close to 1 indicates the filtered image is similar to the reference image. In the expression for SNR, A and σ^2 represent the linear magnitude image and the variance of the background noise region in the linear magnitude image respectively. In the expression for ENL, μ_h and σ_h^2 represent the mean and the variance of the hth homogenous region of interests respectively. In the definition for CNR, μ_b and σ_b^2 represent the mean and the variance of the same background noise region as in SNR and μ_r and σ_r^2 represent the mean and the variance of the rth region of interest which includes the homogeneous regions. In the edge preservation measure, $\nabla^2 M$ and
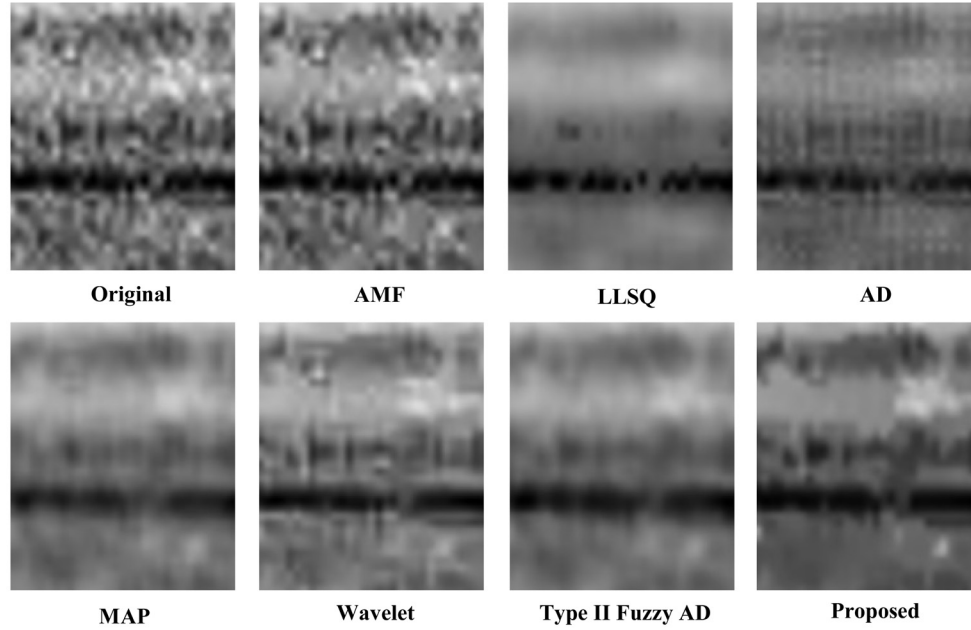
Fig. 5. 3X enlargement of the region in the original OCT image marked with the red box #2 in Fig. 1(b) and processed with the following filters: AMF (adaptive median filter); LLSQ (linear least square estimation); AD (adaptive diffusion); general Wavelet; MAP (maximum a posteriori estimation); Type II fuzzy AD (fuzzy rules controlled adaptive diffusion). The RPE, IS and OS of the photoreceptor layers of the retina appear very sharp and distinct on the image processed with the proposed novel algorithm. In contrast, the same image features appear with low contrast and blurred boundaries on the images processed with the rest of the algorithms.

$\nabla^2 A$ represent the Laplacian operator performed on the original image and the filtered image respectively. Also, $\overline{\nabla^2 M}$ and $\overline{\nabla^2 A}$ represent the mean value of a 3×3 neighbourhood around the pixel location of $\nabla^2 M$ and $\nabla^2 A$ respectively.

Table 1 shows the quantitative performance measure values for the original imaging data and the filtered data. The application of the proposed method resulted in significant performance improvements over the original image and the other tested methods, with SNR improvements of over 17 dB compared to the original image and over 2 dB compared to the next best method, which is the wavelet noise reduction method proposed by Pizurica et al. [9]. This demonstrates the effectiveness of the proposed method for speckle noise suppression. Furthermore, the proposed method produced the second highest edge preservation of the tested methods with an edge preservation score of 0.8860. This demonstrates the effectiveness of the proposed method in terms of preserving image details, which is very important for clinical retinal analysis. The CPU runtime of the novel algorithm is better than most of the tested methods with the exception of the MAP [6] and anisotropic diffusion method [12] methods, but is still recognized as a fast method. Note that the computational complexity of the proposed method is $O(n)$, and as such the computational speed scales linear with the number of pixels in the image, which is a desirable property especially when dealing with high resolution imagery.
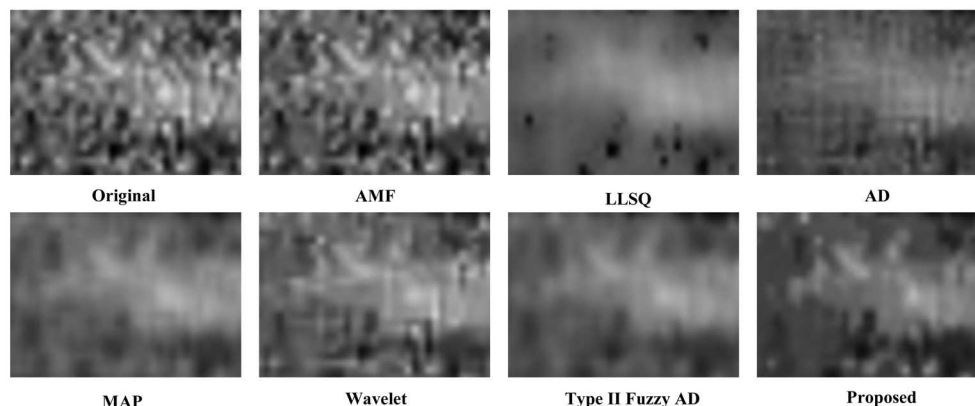
Fig. 6. Magnified view of a choroidal blood vessel, corresponding to the area marked with red box #3 in the original image [Fig. 1(b)] and processed with the different speckle reduction algorithms. AMF adaptive median filter; LLSQ linear least square estimation; AD anisotropic diffusion; general Wavelet; MAP maximum a posteriori estimation; Type II fuzzy AD (fuzzy rules controlled adaptive diffusion). The proposed method results in very clear delineation of the blood vessel walls as compared to the significant blur and / or image artefacts introduced by the other speckle denoising methods.

Table 1. Image quality metrics evaluated for the rat retina image [Fig. 2(b)]. Values are relative to the original image.

Method	SNR (dB)	ENL	CNR (dB)	η	CPU Time (s)
Original	24.2524	44.80	0.9901	N/A	N/A
Adaptive median filter [5]	30.7016	130.80	1.3889	**0.9147**	3.7030
Linear least squares estimation [3]	35.3002	964.80	2.0788	0.5037	1.0470
Wavelet noise reduction [9]	39.9004	**3962.7**	2.8267	0.7213	1.8290
MAP estimation [6]	32.9120	403.40	1.9117	0.0843	**0.3300**
Anisotropic diffusion [12]	30.6513	118.10	2.0446	0.8540	0.5460
Type II Fuzzy anisotropic diffusion [13]	31.9467	266.60	2.1689	0.6232	15.671
Proposed method	**41.9210**	3738.9	**3.6000**	0.8860	0.6359

4. Conclusion

In this paper, we have proposed a novel algorithm for speckle noise reduction in retinal OCT imagery based on log-space general Bayesian estimation. When compared to existing speckle noise reduction methods from research literature, the proposed method demonstrates superior noise suppression and detail preservation. Results using *in-vivo* retinal images show that the proposed method results in SNR improvements of over 17 dB and 2 dB compared to the next best tested method. The proposed method shows great potential in not only improving the overall visual appearance of retinal OCT images, but also the accuracy of image segmentation, registration, and other post-processing algorithms for analyzing OCT tomograms. Furthermore, the novel algorithm has the advantages of providing high contrast and very sharp appearance of zoomed-in sections of the original image, minimal presence of image artefacts, as well as resulting in best performance regardless of the type of image features layered or irregularly shaped structures in the original image. When combined with segmentation algorithms designed for retinal layers or blood vessels, the proposed algorithm can result in improved precision of the
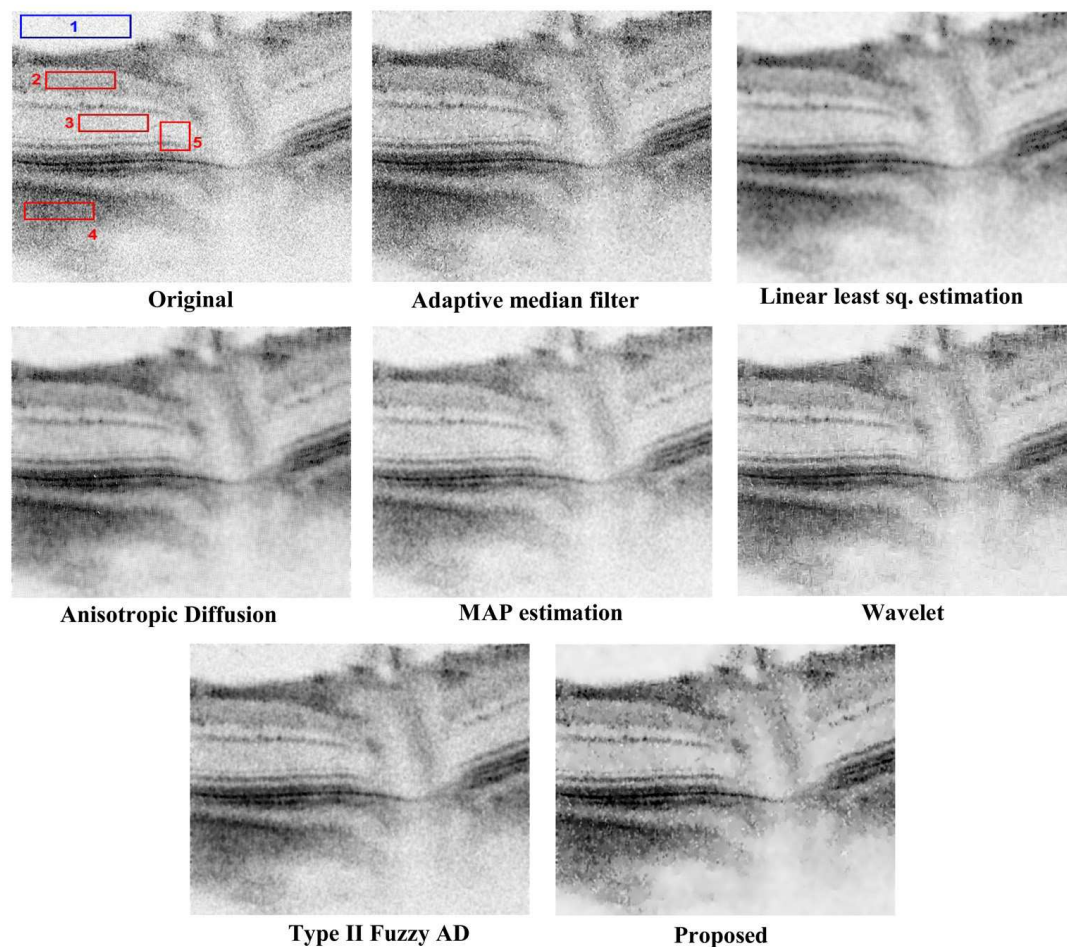
Fig. 7. An OCT image of the rat retina acquired at the optic disc and processed with the following filters: Original image, Adaptive median filter, Linear least square estimation, Anisotropic Diffusion, MAP estimation, general Wavelet, Type II Fuzzy AD, and the new proposed algorithm. The blue and red boxes in the original image mark regions in the image used for quantitative comparison of the performance of all image processing algorithms applied to the original image.

quantitative evaluation of individual retinal layer thickness, or measurement of the blood vessel diameter, a parameter necessary for the precise evaluation of retinal and choroidal blood flow.

Acknowledgment